On the Bimodality of the Wind-Wave Spectrum: Mean Square Slopes and Azimuthal Overlap Integral⬦

LEONEL ROMERO[a] AND KABIR LUBANA[b]

[a] *University of Connecticut, Groton, Connecticut*
[b] *University of California, Santa Barbara, Santa Barbara, California*

ABSTRACT: We present an investigation of the azimuthal bimodality of the wind-wave spectrum for waves shorter than the dominant scale comparing numerical model solutions of developing waves from idealized experiments using WAVEWATCH III (WW3). The wave solutions were forced with the "exact" Webb–Resio–Tracy (WRT) nonlinear energy fluxes and the direct interaction approximation (DIA) with three different combinations of wind input and breaking dissipation parameterizations. The WRT gives larger azimuthal bimodal amplitudes compared to the DIA regardless of wind input/dissipation. The widely used wind input/dissipation parameterizations (i.e., ST4 and ST6) generally give narrow directional distributions with relatively small bimodal amplitudes and lobe separations compared to field measurements. These biases are significantly improved by the breaking dissipation of Romero (R2019). Moreover, the ratio of the resolved cross- to downwind mean square slope is significantly lower for ST4 and ST6 compared to R2019. The overlap integral relevant for the prediction of microseisms is several orders of magnitude smaller for ST4 and ST6 compared to R2019, which nearly agrees with a semiempirical model.

SIGNIFICANCE STATEMENT: Spectral gravity wave models generally cannot accurately predict the directional distribution which impacts their ability to predict the resolved down- and crosswind mean square slopes and the generation of microseisms. Our analysis shows that a directionally narrow spectral energy dissipation, accounting for long-wave–short-wave modulation, can significantly improve the directional distribution of the wind-wave spectrum by coupling to the nonlinear energy fluxes due to wave–wave interactions, which has important implications for improved predictions of the mean square slopes and the generation of microseisms.

KEYWORDS: Wind waves; Air-sea interaction; Gravity waves; Wave breaking

---

1. Introduction

Surface waves affect ocean remote sensing, air–sea exchange processes, and the generation of microseisms. Details of the directional distribution of the energy spectrum of wind-generated gravity waves and the processes that control the directional distribution are poorly understood. The wave energy spectrum becomes azimuthally bimodal away from the spectral peak toward both longer and shorter wavelengths, or wave periods (Young et al. 1995; Ewans 1998; Hwang et al. 2000; Long and Resio 2007). Our study focuses on the latter and its impacts on different metrics of the spectrum.

The first observations of bimodal directional distributions were reported by Young et al. (1995) using a wave gauge array. Later, Ewans (1998) systematically investigated the bimodality of the spectrum of short gravity waves based on extensive buoy measurements. The airborne lidar measurements by Hwang et al. (2000) allowed for a careful analysis of the bimodality of the short waves near full development.

Romero and Melville (2010a) collected airborne lidar measurements of fetch-limited waves in the Gulf of Tehuantepec (GOTEX) providing a detailed characterization of the wavenumber spectrum including the bimodality of the waves shorter than the dominant waves, but the analysis was limited to relatively long waves (18 m and longer). Lenain and Melville (2017) reported airborne lidar measurements of the directional wavenumber spectrum extended into the short gravity range down to 50-cm wavelengths. Their measurements gave bimodal distributions with lobe separations approaching ±90° for the shortest waves resolved. Subsequently, Peureux et al. (2018) also reported extreme bimodal lobe separations approaching ±80° from visible stereo observations.

The directional distribution of the wind-wave spectrum is controlled, to leading order, by nonlinear four-wave resonant interactions (Longuet-Higgins 1976; Young and Van Vledder 1993; Banner and Young 1994; Komen et al. 1984; Toffoli et al. 2010). However, realistic numerical simulations of the wind-wave spectrum with "exact" computations of the nonlinear energy fluxes, specifically the Webb–Resio–Tracy (WRT) algorithm (Tracy and Resio 1982; van Vledder 2006) were shown to give azimuthally bimodal distributions systematically narrower than the observations (Romero and Melville 2010b; Liu et al. 2019). Guimaraes (2018) and Peureux et al. (2018) hypothesized that the bimodality is in part enhanced

---

⬦ Supplemental information related to this paper is available at the Journals Online website: https://doi.org/10.1175/JPO-D-21-0299.s1.

Corresponding author: Leonel Romero, leonel.romero@uconn.edu

due to long-wave–short-wave interactions where short gravity waves preferably break on the crests of long waves in the direction of long-wave propagation. The hypothesis was further supported theoretically with a stability analysis of short-wave modulation by longer waves based on the wave action conservation equation (Peureux et al. 2021).

Building on these ideas and the work by Donelan (2001), Romero (2019) parameterized the spectral energy dissipation due to breaking accounting for short-wave modulation by longer waves where the breaking dissipation for the short waves is preferentially distributed in the direction of the longer dominant waves. This effectively reduces the directional spreading of the spectral dissipation due to breaking while increasing the directional spreading and bimodal lobe separation of the waves shorter than the dominant scale. The wave-breaking model of Romero (2019, hereafter R2019), was implemented in the spectral model WAVEWATCH III (WW3; WW3DG 2019) and tuned against field observations with the wind input of Ardhuin et al. (2010) and both approximate and exact computations of the nonlinear resonant wave–wave interactions (Hasselmann and Hasselmann 1985b; Tracy and Resio 1982; van Vledder 2006). In this study, the model performance with the breaking dissipation R2019 is further analyzed and compared against the two widely used packages: 1) ST4 (Ardhuin et al. 2010) and 2) ST6 (Rogers et al. 2012; Zieger et al. 2015; Liu et al. 2019).

Idealized WW3 solutions of developing waves in deepwater are analyzed focusing on the bimodality of the spectrum for wavenumbers larger than the peak wavenumber, and its impacts on the anisotropy of the resolved mean square slopes, and the azimuthal overlap integral, which is an important metric for the prediction of microseisms (Longuet-Higgins 1950; Hasselmann 1963; Hughes 1976). The work by Alday et al. (2021) shows the impact of the R2019 dissipation on the cross- to downwind mean square slopes. This is further investigated here over a wide range of wind speeds. The manuscript is organized as follows: section 2 describes the model configuration and analysis, section 3 presents the results, which are discussed and summarized in section 4.

2. Methods

Assuming an infinite fetch, the evolution of the directional energy spectrum $F(k, \theta)$ for deep-water waves is governed to leading order by

$$\frac{\partial F(k, \theta)}{\partial t} = S_{in} + S_{nl} + S_{ds}, \qquad (1)$$

where S_{in} is the wind input, S_{nl} corresponds to the energy fluxes due to four-wave resonant interactions, and S_{ds} is the energy dissipation due to breaking. In this study, Eq. (1) was integrated with constant winds for several days using WW3, specifically the source term integration case ww3_ts1 (durationlimited test). Several solutions were generated for surface wind speeds (U_{10}) between 4 and 15 m s^{-1}. The spectrum was discretized with a resolution $\Delta\theta = 10°$ in azimuth and $\Delta k/k = 0.14$ in wavenumber, corresponding to a resolution in frequency

$\Delta f/f = 0.07$ according to the linear dispersion relationship for deep-water waves [$f = (2\pi)^{-1}(gk)^{1/2}$, where g is the gravitational acceleration]. The total number of grid points in azimuth is 36 and 66 in wavenumber. The lowest wavenumber resolved is 0.0016 rad m^{-1} (0.02 Hz) and the upper limit is 10 rad m^{-1} (1.62 Hz) or 60-cm wavelengths. The global integration time step used is 60 s with a minimum dynamical source term integration step of 15 s. Data were analyzed for developing waves with wave age $c_p/u_* < 30$, where c_p is the peak phase speed and u_* is the air-side friction velocity.

The wind input is modeled according to Ardhuin et al. (2010) based on the quasilinear theory of Janssen (1989, 1991) including sheltering at high wavenumbers (Chen and Belcher 2000) due to longer dominant waves and swell dissipation for waves traveling faster than the wind. The nonlinear energy fluxes S_{nl} are computed with the exact algorithm of Tracy and Resio (1982–WRT) implemented in WW3 by van Vledder (2006) and with the standard Direct Interaction Approximation (DIA) of Hasselmann and Hasselmann (1985a,b), which is widely used for applications and operational models. This allows the assessment of S_{nl} impacts on the spectral shape. The wave-breaking dissipation S_{ds} is modeled according to R2019 (Romero 2019; Romero et al. 2012), within the statistical wave breaking framework introduced by Phillips (1985) based on a scaling for Gaussian statistics of the lengths of crest exceeding wave slope criteria (Romero and Melville 2011) while accounting for long-wave–short-wave modulation following the work by Donelan (2001). The wave-breaking statistics model of R2019 was validated against the field measurements of Sutherland and Melville (2013).

The two widely used wind input/dissipation source terms packages in WW3, specifically ST4 (Ardhuin et al. 2010) and ST6 (Rogers et al. 2012; Zieger et al. 2015; Liu et al. 2019), were also considered with both the DIA and WRT nonlinear energy fluxes and the same spectral grid. In other words, all solutions are identical except for the different wind input and dissipation combinations. The ST6 parameterizations were recalibrated recently by Liu et al. (2019) improving the model performance in terms of the integrated parameters and spectral levels within the tail. ST4 is the default wind input/dissipation used operationally at NOAA (Alves et al. 2014). In contrast to ST4, both R2019 and ST6 integrate the resolved spectrum allowing it to evolve freely without a prognostic tail. All ST6 runs were carried out with WW3 v7.14 with the free tail option enabled (SINFC = −1). Both ST4 and R2019 runs were performed with WW3 v5.16.

WW3 integrates the evolution of the spectrum in wavenumber space and outputs the directional frequency spectrum $\psi(f, \theta)$. In this study, the spectra are converted back to wavenumber space $F(k, \theta) = (\partial f/\partial k) \psi(f, \theta) k^{-1}$, here defined such that

$$\langle \eta^2 \rangle = \int F(k, \theta) k \, dk \, d\theta, \qquad (2)$$

with $\langle \eta^2 \rangle$ corresponding to the variance of the surface elevation. Carrying the analysis in wavenumber space allows for a
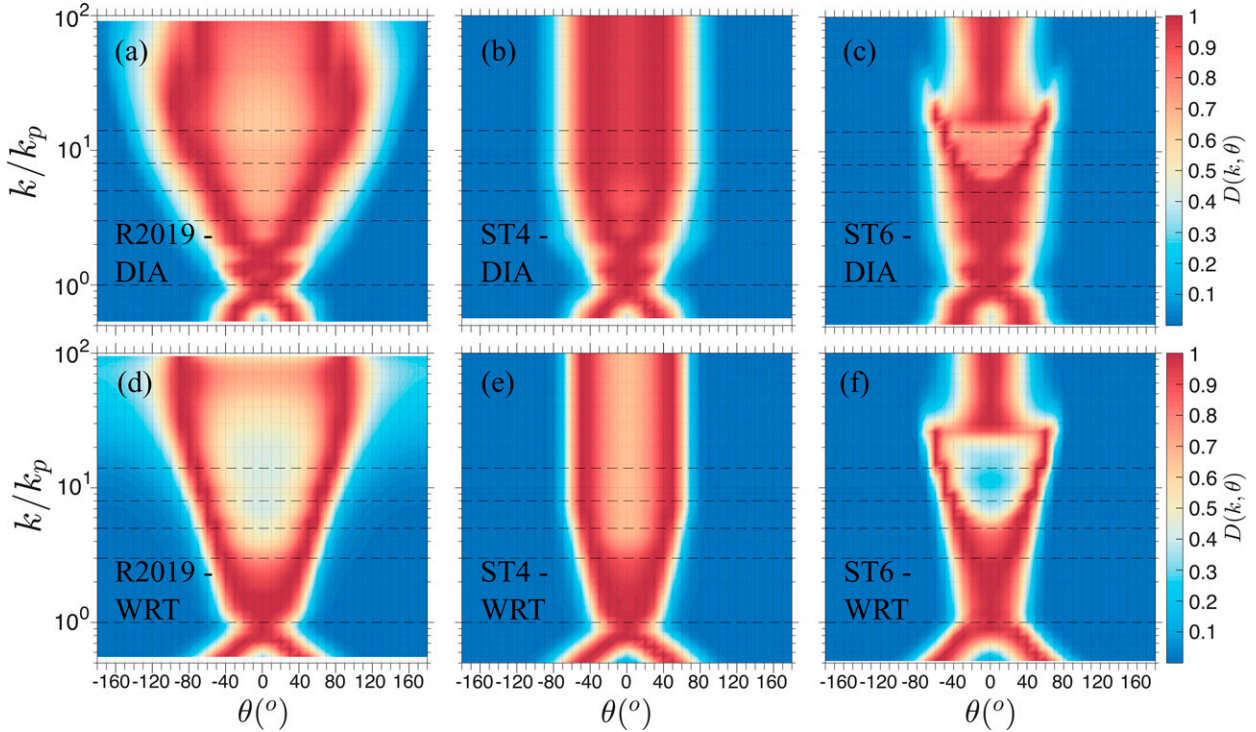
FIG. 1. Directional distributions $D(\theta, k/k_p)$ for (a)–(c) DIA and (d)–(f) WRT solutions forced with (left) R2019, (center) ST4, and (right) ST6. The wave age $c_p/u_* = 15$, and the wind speed $U_{10} = 15$ m s^{-1}. The directional distributions are normalized to have a maximum value of one at each wavenumber (Young et al. 1995; Ewans 1998).

direct comparison with the field measurements on the bimodality of the spectrum by Romero and Melville (2010a). The directional spectrum is decomposed in terms of the directional distribution $D(k, \theta)$ as given by

$$F(k, \theta) = D(k, \theta)\frac{\phi(k)}{k}, \qquad (3)$$

where $\phi(k)$ is the azimuth integrated spectrum according to

$$\phi(k) = \int F(k, \theta)k\, d\theta, \qquad (4)$$

and $D(k, \theta)$ is normalized such that $\int D(k, \theta)d\theta = 1$.

The directional distribution of the wind wave spectrum is unimodal at the spectral peak and bimodal toward both lower and higher wavenumbers (Young et al. 1995; Hwang et al. 2000; Long and Resio 2007; Romero and Melville 2010a). The bimodality is often characterized with respect to the average lobe separation $\theta_{\text{lobe}}(k)$ and amplitude $r_{\text{lobe}}(k)$ defined according to

$$\theta_{\text{lobe}}(k) = \frac{|\theta_-(k)| + |\theta_+(k)|}{2}, \qquad (5)$$

$$r_{\text{lobe}}(k) = \frac{1}{2}\frac{D(k, \theta_-) + D(k, \theta_+)}{D(k, \overline{\theta})}, \qquad (6)$$

where $\theta_\pm(k)$ are azimuthal maxima on each side of the spectrum relative to the mean wave direction $\overline{\theta}(k)$ given by

$$\overline{\theta}(k) = \text{atan}\left[\frac{\int \sin(\theta)F(k, \theta)k\, d\theta}{\int \cos(\theta)F(k, \theta)k\, d\theta}\right]. \qquad (7)$$

In this study, the spectrum is symmetric about the wind direction θ_w and $\overline{\theta}(k) = \theta_w$ across the spectrum. The lobe maxima $\theta_\pm(k)$ are calculated using the weighted integral

$$\theta_\pm(k) = \frac{\int_0^{\pm\pi} F^4(k, \theta)(\pm\theta)d\theta}{\int_0^{\pm\pi} F^4(k, \theta)d\theta}, \qquad (8)$$

which is based on the method used by Young (1995) to determine the peak frequency. The weighted integral yields relatively smooth curves of $\theta_{\text{lobe}}(k)$ not locked to the azimuthal model grid.

The bimodality of the spectrum directly impacts other metrics of the spectrum, including the ratio of the cross- to downwind mean square slope mss$_1$/mss$_2$ and the azimuthal overlap integral (Munk 2009). By definition, the total mean square slope mss = mss$_1$ + mss$_2$ with down- and crosswind components given by

$$\text{mss}_1 = \iint F(k, \theta)(k\cos\theta)^2 k\, dk\, d\theta \qquad (9)$$

$$\text{mss}_2 = \iint F(k, \theta)(k\sin\theta)^2 k\, dk\, d\theta, \qquad (10)$$
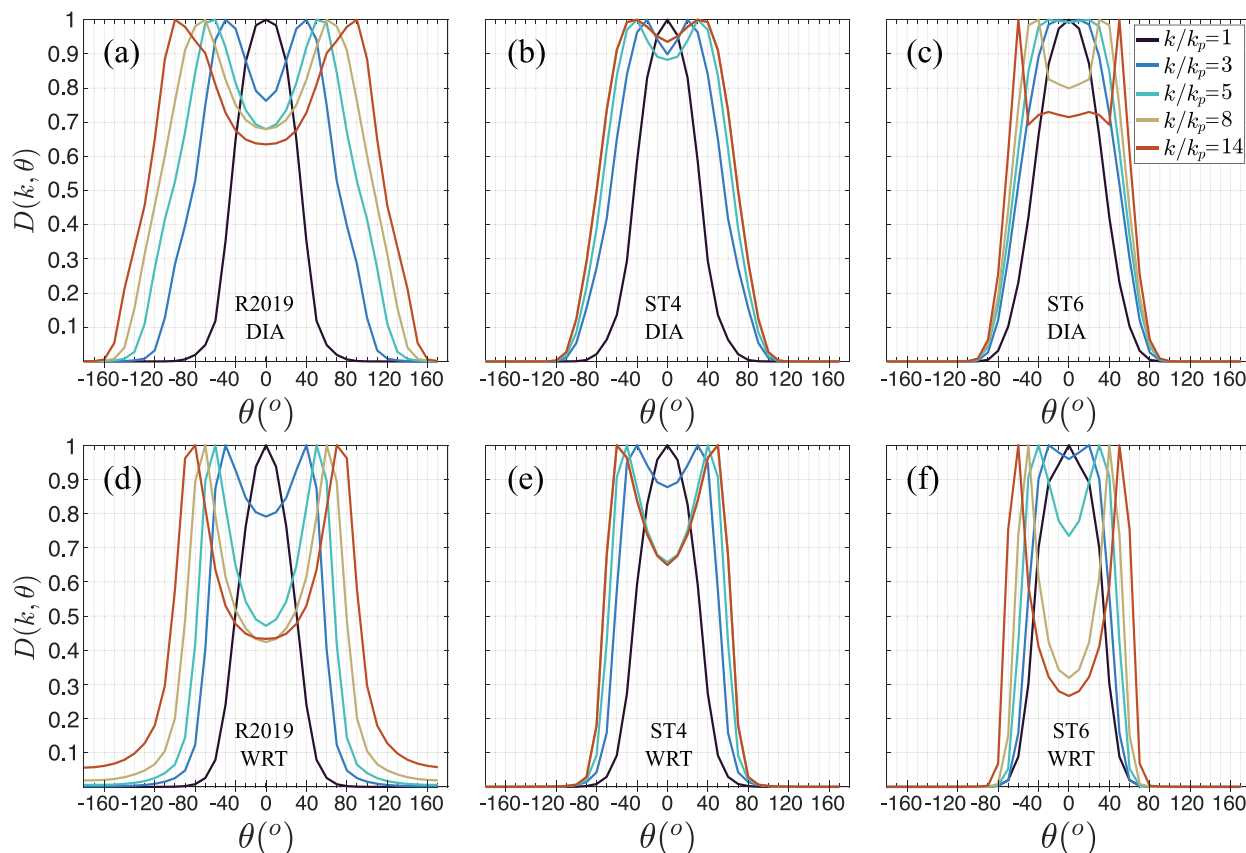
FIG. 2. (a)–(f) Directional distributions $D(\theta, k/k_p)$ at k/k_p 1, 3, 5, 8, and 14, which correspond to the horizontal dashed lines in Fig. 1.

respectively. The overlap integral $I(k)$ defined as

$$I(k) = \int D(k, \theta) D(k, \theta + \pi) d\theta, \qquad (11)$$

is a measure of the fraction of energy that travels in opposite directions. Waves traveling in opposite direction result in pressure fluctuations at the bottom of the ocean contributing to microseisms. The amount of microseismic energy is directly proportional to the overlap integral (Longuet-Higgins 1950; Hughes 1976).

3. Results

The results are presented in three subsections comparing the model solutions among themselves and field observations, starting with a characterization of the directional distribution and bimodality, followed by an analysis of the anisotropy of the mean square slopes and the azimuthal overlap integral.

a. Directional distribution

Examples of directional distributions from wave model solutions forced with the different wind input/dissipation packages and both approximate (DIA) and exact (WRT) computations of the nonlinear energy fluxes for 15 m s^{-1} winds and a wave age c_p/u_* of 15 are shown in Figure 1 with

corresponding individual cross sections at $k/k_p = 1, 3, 5, 8$, and 14 shown in Fig. 2. The bimodal distributions are evident across all solutions away from the spectral peak. As expected, the bimodality is enhanced in WRT solutions compared to the DIA regardless of the wind input/dissipation. Both ST4 and ST6 give significantly narrower bimodal separations compared to R2019. For example, the lobe separation of WRT solutions at $k/k_p = 14$ is $\pm 70°$ for R2019 compared to $\pm 50°$ for both ST4 and ST6. The relatively large bimodal lobe separations of R2019 solutions becomes even wider with the DIA, reaching $\pm 90°$ at $k/k_p = 14$. Lobe separations of comparable magnitude were reported from airborne lidar observations (Lenain and Melville 2017) and visible stereo measurements (Peureux et al. 2018). The lobe separations of R2019 solutions are wider compared to ST4 and ST6 because the energy dissipation is azimuthally much narrower. This is demonstrated in Fig. 3 showing $S_{ds}(k, \theta)$ for the 15 m s^{-1} WRT solutions at different wave ages and the different dissipation formulations.

The lobe separation and amplitude dependence on the wavenumber relative to the spectral peak and wave age c_p/u_* are analyzed in Figs. 4 and 5, respectively. The lobe separations $\theta_{lobe}(k/k_p)$ are qualitatively similar between DIA and WRT solutions for a given wind input/dissipation. The differences between R2019, ST4, and ST6 solutions are significant. There is a general trend among all solutions giving, on
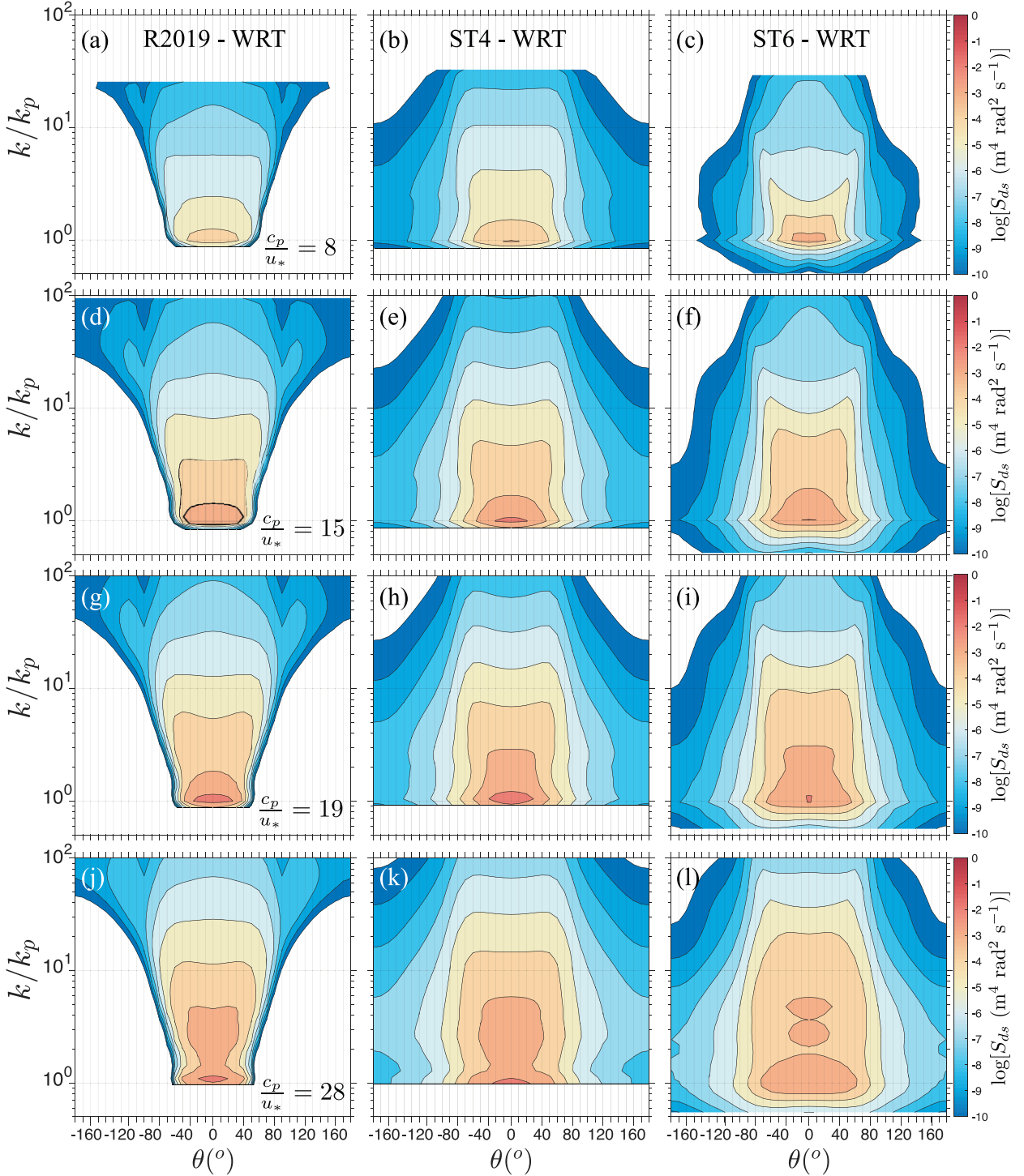
FIG. 3. Directional energy dissipation $S_{ds}(k, \theta)$ for WRT solutions forced by 15 m s^{-1} winds at wave ages $c_p/u_* =$ (a)–(c) 8, (d)–(f) 15, (g)–(i) 19, and (j)–(l) 28. Shown are (left) R2019, (center) ST4, and (right) ST6.

average, larger lobe separations for younger seas, and vice versa. The lobe separation generally increases with increasing wavenumber k/k_p, except for ST6 at the lowest wave age, which is consistent with the transition from bimodal to

unimodal at large wavenumbers in Figs. 1c and 1f. As shown in Fig. 1, R2019 gives larger lobe separations compared to both ST4 and ST6, regardless of the nonlinear energy fluxes. The lobe separations for R2019 reach about 70° and
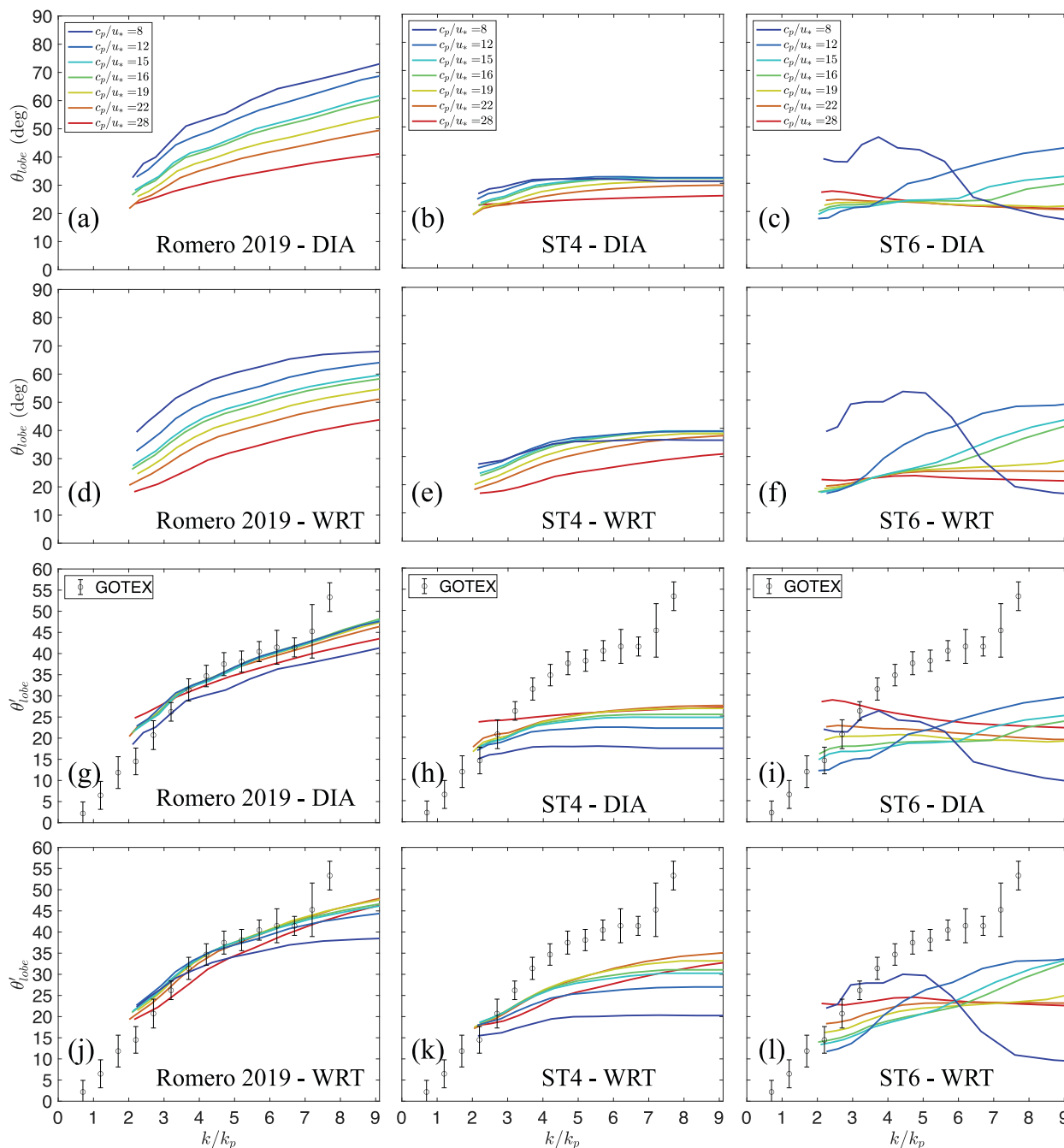
FIG. 4. Bimodal lobe separation $\theta_{lobe}(k/k_p)$ for the (a)–(c) DIA and (d)–(f) WRT solutions, forced with 15 m s^{-1} winds color coded by wave age. The data near the spectral peak $(1 > k/k_p < 2)$ are omitted for clarity since the spectra in that region are generally unimodal or weakly bimodal. Shown are (left) R2019, (center) ST4, and (right) ST6. (g)–(l) The resulting distributions scaled by $0.2\,(c_p/u_*)^{1/2}$ and compared against GOTEX measurements Romero and Melville (2010a).

42° at $k/k_p = 9$ for wave ages between 8 and 28. In contrast, ST4 gives θ_{lobe} between 40° and 30° and ST6 between 50° and 20° at $k/k_p = 9$.

The lobe amplitudes $r_{lobe}(k/k_p)$ in Fig. 5 show patterns that are qualitatively similar to those in Fig. 4 with larger values for the WRT solutions compared to the DIA. The lobe amplitudes for R2019 show a decreasing trend with wave age, nearly independent of k/k_p for the DIA and on average monotonically increasing with k/k_p for WRT. The R2019 lobe amplitudes reach values of up to 2.5 and 2 for WRT and DIA, respectively. The lobe amplitudes are smallest for ST4, nearly independent of wave age, and relatively larger for WRT
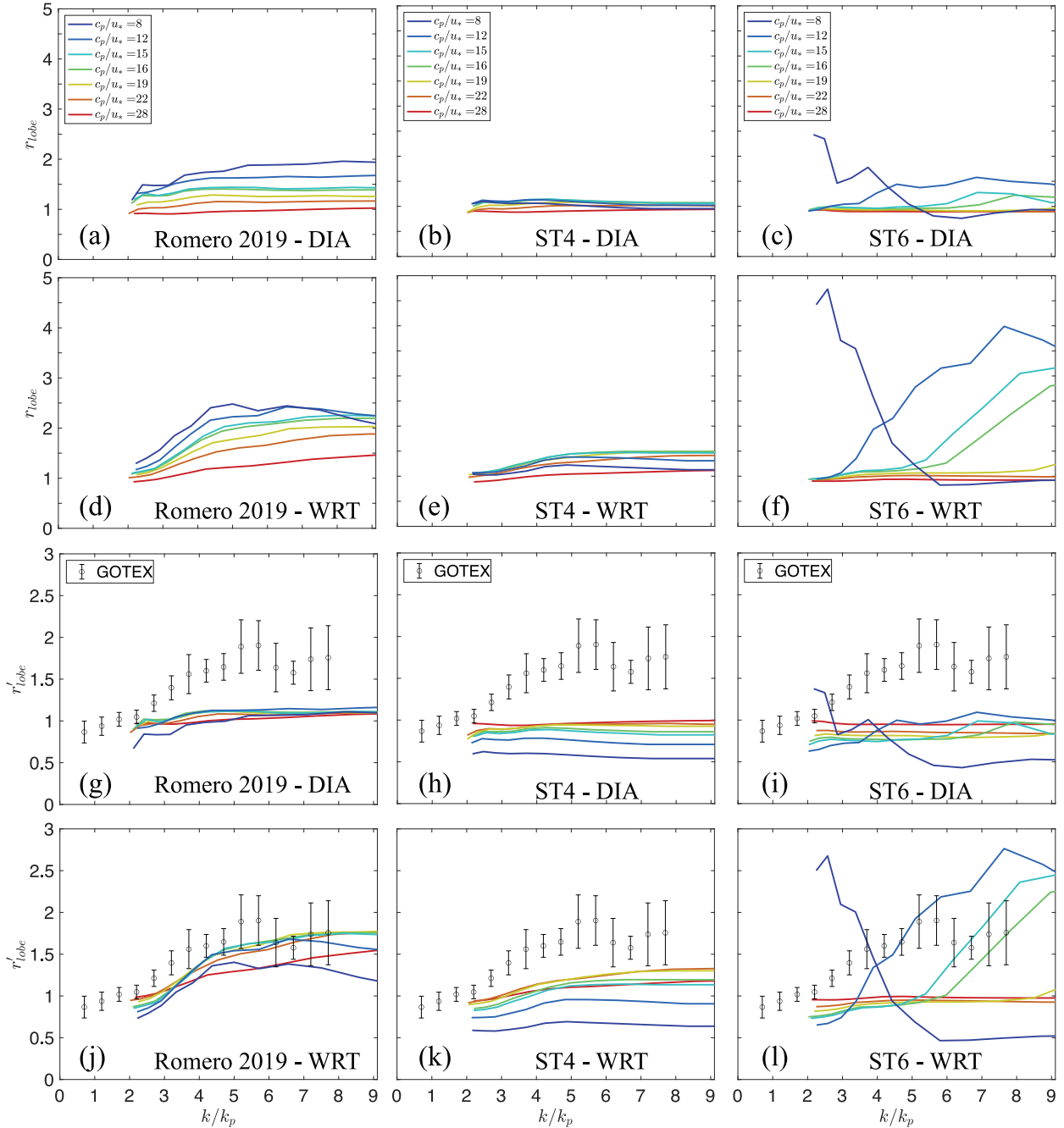
FIG. 5. As in Fig. 4, but for the relative lobe amplitude $r_{\text{lobe}}(k/k_p)$.

compared to DIA. The ST6 solutions forced with exact non-linear energy fluxes (WRT) give the largest lobe amplitudes reaching values of up to 4.5 for the lowest wave age. Both DIA and WRT ST6 solutions show a decreasing trend with increasing wave age for $8 < c_p/u_* < 19$. For $c_p/u_* = 8$ the lobe amplitudes r_{lobe} are nonmonotonic but generally decreasing with increasing k/k_p.

Romero and Melville (2010a) reported an empirical scaling that collapsed the observed wave age dependence of the

bimodal separation and amplitude. The scaling consisted of a factor proportional to $(c_p/u_*)^{1/2}$ with a proportionality constant arbitrarily set to 0.2, such that the scaling $\mathcal{F} = 0.2(c_p/u_*)^{1/2}$ would keep the overall magnitude of the scaled variables comparable to the unscaled ones. The scaled lobe separation and amplitude, defined as $\theta'_{\text{lobe}}(k/k_p) = \mathcal{F}\theta_{\text{lobe}}(k/k_p)$ and $r'_{\text{lobe}}(k/k_p) = \mathcal{F}r_{\text{lobe}}(k/k_p)$ are shown in Figs. 4g–l and Figs. 5g–l, respectively, and compared to the GOTEX observations. The R2019 solutions, both DIA and
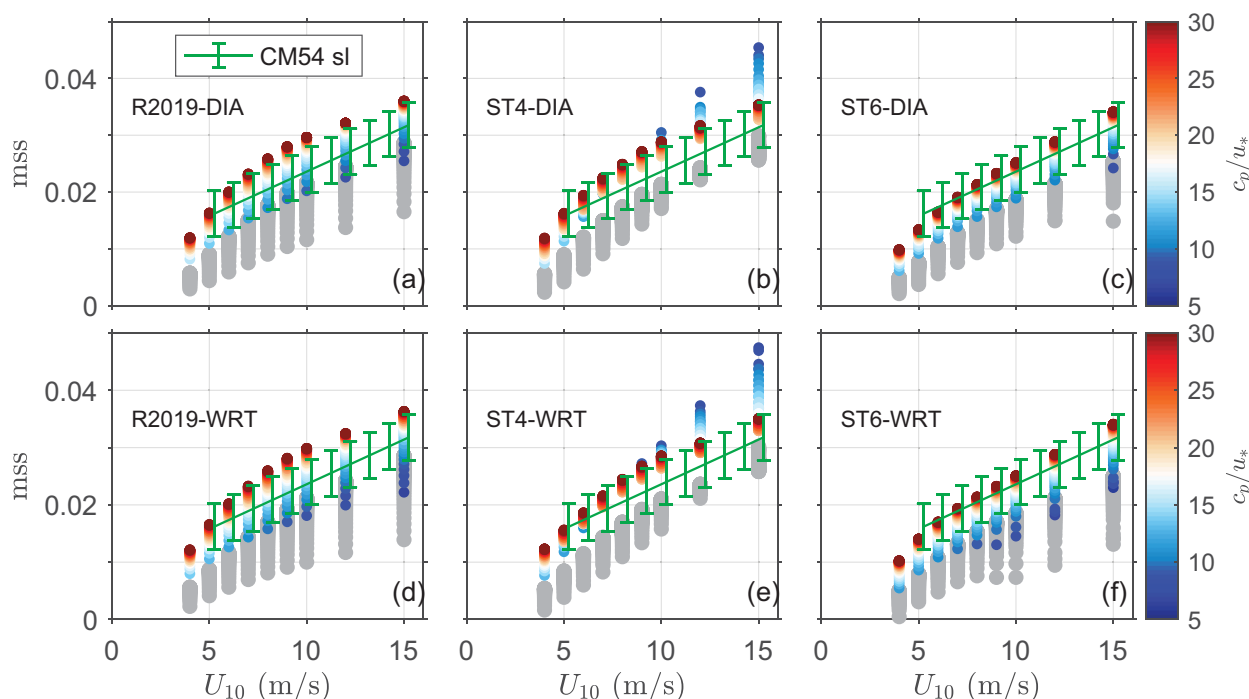
FIG. 6. Resolved mean square slope mss as a function of wind speed from solutions forced with the (a)–(c) DIA and (d)–(f) WRT. The solid green lines with error bars are the field measurements by Cox and Munk (1954a) in slick conditions. Shown are (left) R2019, (center) ST4, and (right) ST6. The gray dots show the corresponding mss limiting the integration to 4 rad m^{-1} (1.5-m wavelengths) or 1 Hz.

WRT, collapse for both $\theta'_{\mathrm{lobe}}(k/k_p)$ and $r'_{\mathrm{lobe}}(k/k_p)$. The scaled lobe separations for R2019 are in good agreement with GOTEX observations for both the DIA and WRT. However, the empirical $r'_{\mathrm{lobe}}(k/k_p)$ data are only approximately matched by the R2019 WRT solution. The R2019 DIA solution gives much lower values of $r'_{\mathrm{lobe}}(k/k_p)$. In contrast, neither ST4 nor ST6 collapse nor match the GOTEX measurements for both $\theta'_{\mathrm{lobe}}(k/k_p)$ and $r'_{\mathrm{lobe}}(k/k_p)$. These results for ST4 and ST6 from Figs. 4 and 5 are qualitatively similar to those in Fig. S10 of Liu et al. (2019) for solutions with higher directional resolution ($\Delta\theta = 5°$) and forced by stronger winds (20 m s^{-1}). We carried out additional experiments with stronger winds (20 m s^{-1}) and different spectral resolutions ($\Delta f/f = 0.1$ and $\Delta\theta = 5°$). In general, we find that while the bimodality of R2019 and ST4 solutions remain qualitatively similar, WRT-ST6 solutions are most sensitive to the spectral resolution giving on average larger lobe separations and amplitudes for $\Delta\theta = 5°$ compared to $\Delta\theta = 10°$ and for $\Delta f/f = 0.07$ compared to $\Delta f/f = 0.1$. The interested reader may refer to the supplemental material (Figs. S1–S4 in the online supplemental material).

The relatively good agreement between the R2019 WRT solutions and the GOTEX empirical scaling is a significant improvement over the previous modeling efforts (Romero and Melville 2010b; Liu et al. 2019) where θ' was shown to collapse but with consistently smaller lobe separations. The agreement between the R2019 solutions and the GOTEX bimodality scaling is in part because the dissipation was tuned against the GOTEX scaling. However, the model performance was not shown in R2019 and is demonstrated here. In the next subsections, the model performance is further analyzed with other metrics that are directly related to the directional distribution, specifically the mean square slopes and overlap integral.

b. Mean square slopes

A metric directly related to the directional distribution is the anisotropy of the mean square slopes, specifically the ratio of the down- to crosswind mean square slope (Munk 2009). Cox and Munk (1954a,b) reported novel measurements of the sea surface slope statistics using airborne aerial images of sun glint proving empirical relationships of the mean square slopes as functions of wind speed. The Cox and Munk (1954a) mean square slope measurements were further confirmed by Bréon and Henriot (2006) and Lenain et al. (2019) using satellite visible imagery and lidar observations, respectively. Although the total mean square slope is dominated by the gravity-capillary part of the spectrum, the contribution due to gravity waves is significant (Cox and Munk 1954a). Here the mean square slopes of the resolved gravity wave spectrum are analyzed and compared to the measurements by Cox and Munk (1954a) for slick conditions, hereafter referred to as CM54sl. The comparison is qualitative because it is not exactly known the exact cutoff wavenumber for slick conditions, while the upper limit of the solutions is 10 rad m^{-1} or 60 cm.

The resolved mss color-coded according to wave age is plotted as a function of wind speed compared to CM54sl for
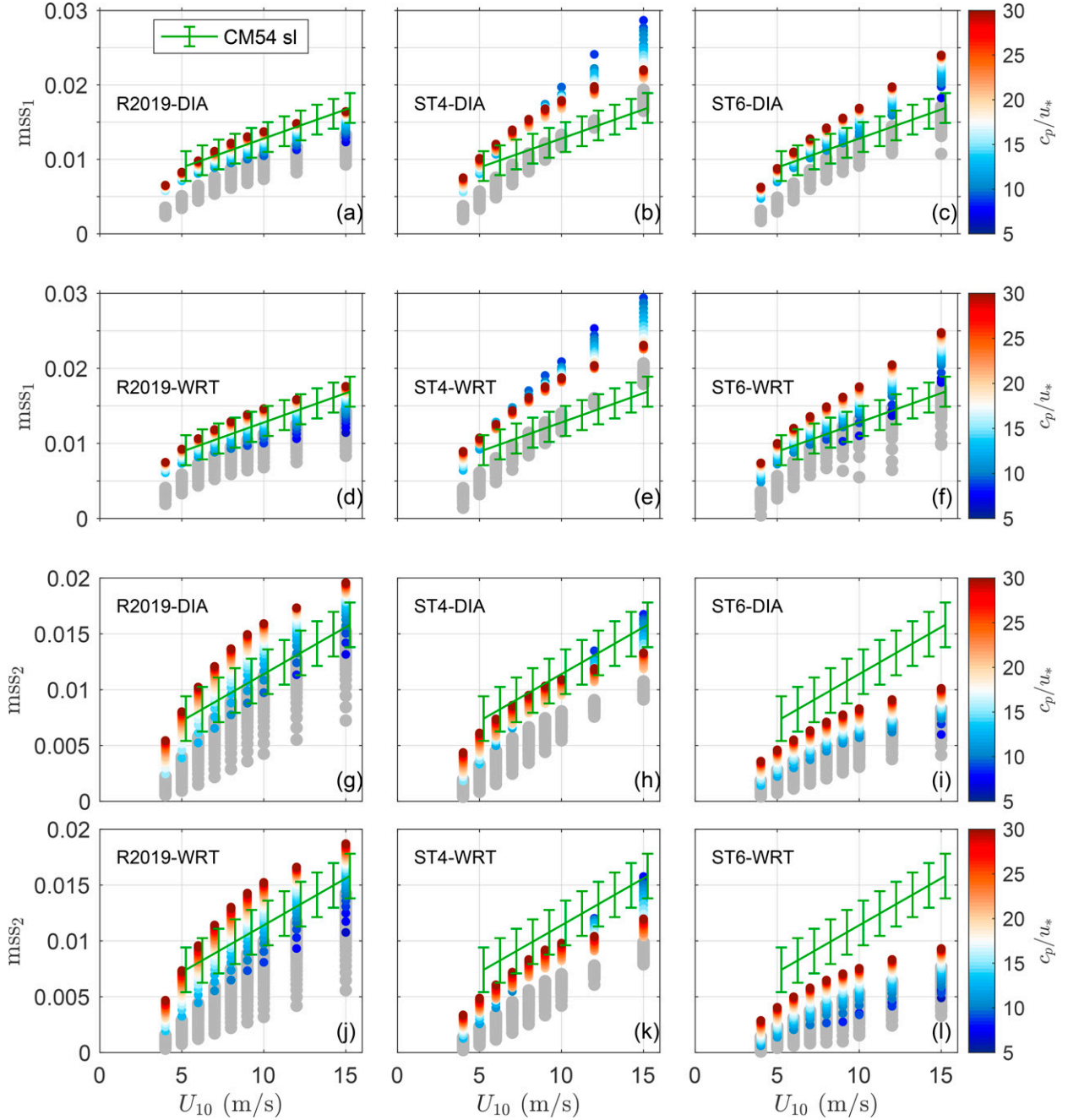
FIG. 7. Resolved mean square slope components (a)–(f) downwind (mss_1) and (g)–(l) crosswind (mss_2) as a function of wind speed from solutions forced with different wind input/dissipation combinations (R2019, ST4, and ST6) and nonlinear energy fluxes (DIA and WRT) as labeled. The solid green lines with error bars are the field measurements by Cox and Munk (1954a) in slick conditions. The gray dots show the corresponding mss limiting the integration to 4 rad m^{-1} (1.5-m wavelengths) or 1 Hz.

WRT and DIA solutions in Figs. 6a–c and 6d–f, respectively. All datasets show substantial variability due to wave age, qualitatively within the uncertainty bounds of CM54sl except for ST4 at low wave ages, with small differences due to the different computations of the nonlinear energy fluxes (WRT versus DIA). R2019 gives the largest mss values for older

waves. Both R2019 and ST6 show an increase in mss with wave age. In contrast, ST4 shows two patterns with mss increasing with increasing wave age at low winds and reversing at high winds where mss decreases with wave age.

The mss slope components (mss_1, mss_2) are plotted individually versus wind speed in Figs. 7a–f and 7g–l, corresponding
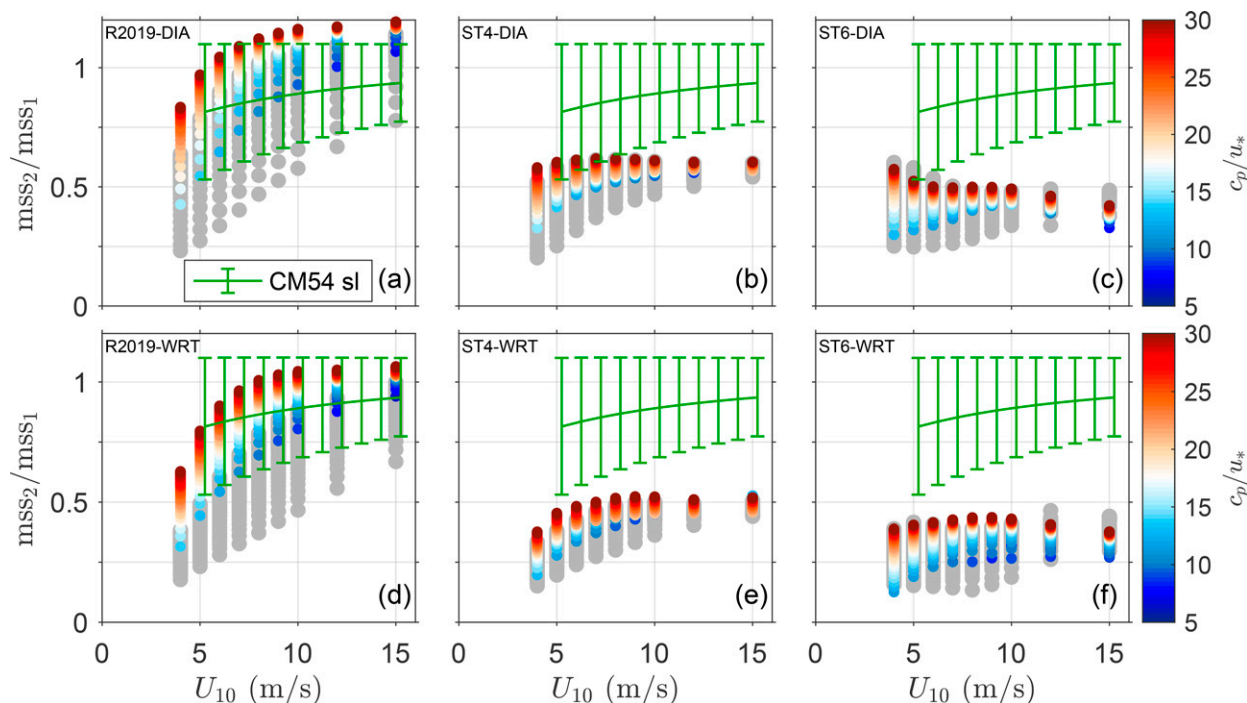
FIG. 8. Ratio of resolved cross- to downwind mean square slopes (mss_2/mss_1) as a function of wind speed from solutions forced with the (a)–(c) DIA and (d)–(f) WRT. The solid green lines with error bars are the field measurements by Cox and Munk (1954a) in slick conditions. Shown are (left) R2019, (center) ST4, and (right) ST6. The gray dots show the corresponding mss limiting the integration to 4 rad m^{-1} (1.5-m wavelengths) or 1 Hz.

to the downwind (mss_1) and crosswind component (mss_2), respectively. The DIA (Figs. 7a–c,g–i) and WRT (Figs. 7d–f,j–l) solutions are shown for the different wind input/dissipation packages. The exact computation of the nonlinear energy fluxes (WRT) generally gives larger downwind and smaller crosswind mean square slopes for all the cases considered. R2019 shows good agreement with CM54sl for both components. ST4 overestimates mss_1 and approximately matches the observed mss_2. In contrast, ST6 approximately matches mss_1 for young waves but also significantly underestimates mss_2 compared to CM54sl. This shows that the relatively narrower bimodal lobe separations give smaller mss_2 relative to mss_1. This is better shown plotting ratio mss_2/mss_1 versus wind speed in Figs. 8a–c and 8d–f for the WRT and DIA solutions, respectively. The R2019 WRT solutions show good agreement against CM54sl generally within error bars, while the R2019 DIA solutions are biased high significantly exceeding CM54sl at higher winds ($U_{10} > 7$ m s^{-1}). In contrast, both ST4 and ST6 largely underestimate the ratio mss_2/mss_1 compared to CM54sl.

From further analysis on the impact of model resolution, we found that the mean square slopes (mss_1 and mss_2) are not very sensitive (generally within 1%–2%) to small changes of the spectral resolution in frequency (i.e., $\Delta f/f = 0.1$ compared to 0.07) regardless of the forcing. Similarly, increasing the azimuthal resolution from 10° to 5° has negligible impacts on the mean square slopes of DIA solutions. In contrast, WRT solutions are affected the most by the increase in azimuthal

spectral resolution ($\Delta\theta = 5°$) giving larger mss_2 and the ratio mss_2/mss_1 by about 3% for both ST4 and R2019, whereas for ST6 mss_2/mss_1 and mss_2 increase by 4.4% and 5.4%, respectively.

The impacts of using the more common model grid upper frequency limit of 1 Hz on the computations of the mean square slopes are shown in Figs. 6–8 with solid gray circles. Limiting the integration 1 Hz compared to 1.6 Hz gives lower mss_1 values on average by about 10%–50% and lower mss_2 values by about 10%–25%. This is demonstrated in the supplemental material (Fig. S5) through direct comparisons.

c. Overlap integral

Longuet-Higgins (1950) demonstrated theoretically that surface gravity wave groups traveling in opposite directions can generate pressure fluctuations at the bottom of the ocean at twice the frequency of the surface waves ($\sigma = 2\pi f$). Following Farrell and Munk (2008),[1] the acoustic pressure spectrum for a given surface wave spectrum and overlap integral corresponds to

$$\phi_P(\sigma_p) = \frac{\pi}{8}\left(\frac{\rho_w}{c_s}\right)^2 \sigma_p^6 k^{-1} \phi^2(k) \frac{\partial k}{\partial\sigma} I(k), \qquad (12)$$

where ρ is the seawater density, $c_s = 1500$ m s^{-1} is the speed of sound in water, and $\sigma_p = 2\sigma$ is the acoustic frequency

---

[1] Note Eq. (12) differs from Eq. (5) in Farrell and Munk (2008) based on their definition of $F_\eta(k) = \int F(k,\theta)d\theta = \phi(k)k^{-1}$.
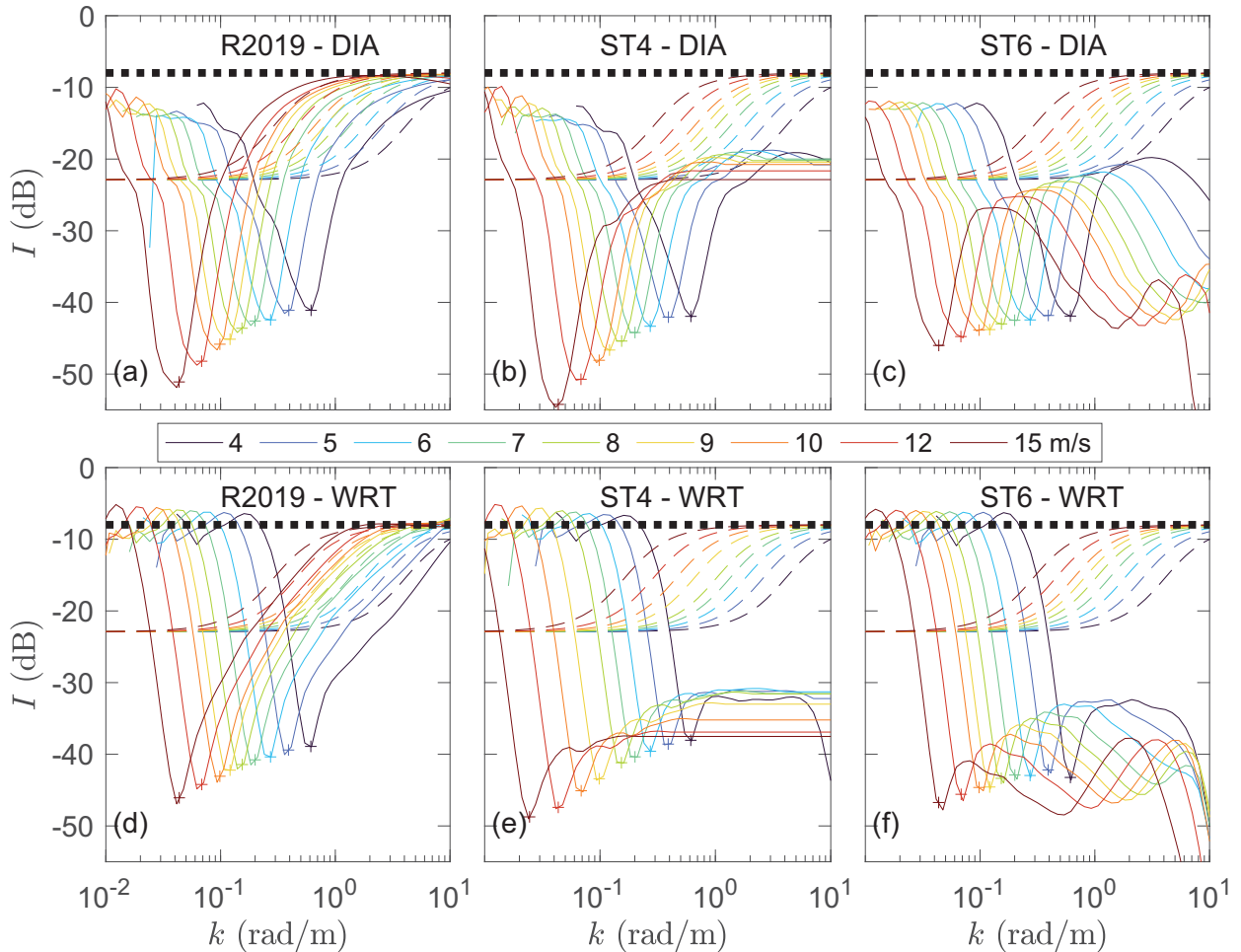
FIG. 9. Overlap integral $I(k)$ comparing (a)–(c) DIA and (d)–(f) WRT solutions with wind input/dissipation for $c_p/U_{10} = 1$ and wind speeds between 4 and 15 m s^{-1}. The dashed lines correspond to the semiempirical model by DLNAW and the dotted black lines show the expected value for an isotropic spectrum. The plus signs show $I(k_p)$ near the minima. Shown are (left) R2019, (center) ST4, and (right) ST6.

(Hasselmann 1963; Hughes 1976). In this section we describe an analysis of the overlap integral $I(k)$ from the various solutions comparing them against a semiempirical analytical model. Duennebier et al. (2012, hereafter DLNAW), collected simultaneous wind, wave, and near-bottom acoustic measurements to investigate the generation of microseisms. Combining measurements of the acoustic spectrum ϕ_p with an empirical model of the wave spectrum, DLNAW inverted the overlap integral from Eq. (12) and parameterized it according to

$$I_{dB}(k) = 9.5\arctan[0.04(k/k_p)^{1.7}] - 22.9, \qquad (13)$$

where $k_p = g/U_{10}^2$ is the peak wavenumber assuming fully developed seas, and the subscript dB indicates units of decibels.

The overlap integral $I(k)$ directly computed from wave solutions near "full" development $c_p/U_{10} = 1$ are plotted in Fig. 9 comparing the different physics against DLNAW for wind speeds between 4 and 15 m s^{-1}. The model solutions exhibit minima near the spectral peak where the spectra are narrowest and generally increase away from the peak. The semiempirical model monotonically increases with wavenumber at intermediate scales approaching constant values toward low and high wavenumbers. The relatively large values of $I(k)$ at low wavenumbers for the DLNAW model are attributed to wave energy from shoreline reflections not accounted for in the idealized numerical solutions. At wavenumbers much larger than the spectral peak the model solutions are significantly lower compared to DLNAW, except for R2019. In general, WRT solutions give lower values $I(k)$ compared to the DIA. Both DLNAW and R2019 approach the value of −8 dB [$10\log_{10}(1/2\pi)$] consistent with that of an isotropic spectrum. Increasing the directional resolution to 5° slightly increases the overlap integral of solutions forced by WRT (not shown). The much larger overlap integral values given by R2019 compared to ST4 and ST6 are due to the strong bimodality of the spectrum with large lobe separations, which is consistent with the ideas discussed by Munk (2009).

4. Discussion and conclusions

We presented an analysis of numerical solutions produced with WW3 for idealized conditions forced with the approximate (DIA) and exact (WRT) nonlinear energy fluxes and different wind input/dissipation, specifically the widely used ST4 and ST6 packages, and R2019. WRT solutions give consistently larger bimodal amplitudes compared to those obtained with the DIA, independent of wind input/dissipation. The R2019 solutions with WRT give the best agreement against the GOTEX empirical scaling of the lobe amplitudes and separations. ST4 gives much weaker lobe amplitudes and separations regardless of the nonlinear energy fluxes. Similarly, ST6 gives lobe separations generally narrower than the GOTEX observations. ST6 gives the largest lobe amplitudes at lower wave ages with nonmonotonic trends for both the lobe amplitudes and lobe separation with respect to the scale and wave age.

Further analysis shows that all model solutions give total resolved mean square slope (mss) versus wind speed comparable to Cox and Munk (1954a) in slick conditions (CM54). However, the individual components versus wind speed are generally not in agreement with CM54, except for R2019. ST4 and ST6 give mss_1 and mss_2 generally larger and smaller than CM54, respectively, with the exception of ST6 mss_1 for young waves which approximately match CM54. Consequently, the ratio mss_2/mss_1 is significantly lower for ST4 and ST6 compared to R2019 and CM54. DIA solutions generally give larger mean square slope ratios compared to WRT. Similarly, the overlap integral computed from model solutions is significantly smaller at high wavenumbers for ST4 and ST6 compared to R2019, which gives values comparable to the semiempirical findings by DLNAW. Regardless of the physics, the DIA generally gives larger overlap integral values compared to WRT.

The results from the study suggest that directional distribution produced by R2019 is more realistic compared to ST4 and ST6 as determined by three independent metrics and datasets (Cox and Munk 1954a; Romero and Melville 2010a; DLNAW). The main difference between R2019 and the other models is the relatively narrower spreading of the energy dissipation due to breaking which couples with the nonlinear energy fluxes due to wave–wave resonant interactions leading to a wider spectrum and stronger bimodality. A similar effect could result from a wider or bimodal wind forcing like Phillips (1957) resonance due to pressure fluctuations. Ultimately as shown by Alves and Banner (2003), all three terms combined (wind input, nonlinear energy fluxes, and dissipation) shape the directional distribution of the spectrum of the short gravity waves. Further work is needed to better understand the controls on the directional distribution of short gravity waves.

REFERENCES

Alday, M., M. Accensi, F. Ardhuin, and G. Dodet, 2021: A global wave parameter database for geophysical applications. Part 3: Improved forcing and spectral resolution. *Ocean Modell.*, **166**, 101848, https://doi.org/10.1016/j.ocemod.2021.101848.

Alves, J.-H. G., and M. L. Banner, 2003: Performance of a saturation-based dissipation-rate source term in modeling the fetch-limited evolution of wind waves. *J. Phys. Oceanogr.*, **33**, 1274–1298, https://doi.org/10.1175/1520-0485(2003)033<1274:POASDS>2.0.CO;2.

——, A. Chawla, H. L. Tolman, D. Schwab, G. Lang, and G. Mann, 2014: The operational implementation of a Great Lakes wave forecasting system at NOAA/NCEP. *Wea. Forecasting*, **29**, 1473–1497, https://doi.org/10.1175/WAF-D-12-00049.1.

Ardhuin, F., and Coauthors, 2010: Semiempirical dissipation source functions for ocean waves. Part I: Definition, calibration, and validation. *J. Phys. Oceanogr.*, **40**, 1917–1941, https://doi.org/10.1175/2010JPO4324.1.

Banner, M. L., and I. R. Young, 1994: Modeling spectral dissipation in the evolution of wind waves. Part I: Assessment of existing model performance. *J. Phys. Oceanogr.*, **24**, 1550–1571, https://doi.org/10.1175/1520-0485(1994)024<1550:MSDITE>2.0.CO;2.

Bréon, F. M., and N. Henriot, 2006: Spaceborne observations of ocean glint reflectance and modeling of wave slope distributions. *J. Geophys. Res.*, **111**, C06005, https://doi.org/10.1029/2005JC003343.

Chen, G., and S. E. Belcher, 2000: Effects of long waves on wind-generated waves. *J. Phys. Oceanogr.*, **30**, 2246–2256, https://doi.org/10.1175/1520-0485(2000)030<2246:EOLWOW>2.0.CO;2.

Cox, C., and W. Munk, 1954a: Measurement of the roughness of the sea surface from photographs of the sun's glitter. *J. Opt. Soc. Amer.*, **44A**, 838–850, https://doi.org/10.1364/JOSA.44.000838.

——, and ——, 1954b: Statistics of the sea surface derived from sun glitter. *J. Mar. Res.*, **13**, 198–227.

Donelan, M. A., 2001: A nonlinear dissipation function due to wave breaking. *Proc. of ECMWF Workshop on Ocean Wave Forecasting, 2–4 July*, ECMWF, Reading, United Kingdom, 87–94, https://www.ecmwf.int/node/9094.

Duennebier, F. K., R. Lukas, E. M. Nosal, J. Aucan, and R. A. Weller, 2012: Wind, waves, and acoustic background levels at Station ALOHA. *J. Geophys. Res.*, **117**, C03017, https://doi.org/10.1029/2011JC007267.

Ewans, K. C., 1998: Observations of the directional spectrum of fetch-limited waves. *J. Phys. Oceanogr.*, **28**, 495–512, https://doi.org/10.1175/1520-0485(1998)028<0495:OOTDSO>2.0.CO;2.

Farrell, W. E., and W. Munk, 2008: What do deep sea pressure fluctuations tell about short surface waves? *Geophys. Res. Lett.*, **35**, 8–11, https://doi.org/10.1029/2008GL035008.

Guimaraes, P. V., 2018: Sea surface and energy dissipation. Ph.D. thesis, Université Bretagne Loire, 204 pp.

Hasselmann, K., 1963: A statistical analysis of the generation of microseisms. *Rev. Geophys.*, **1**, 177–210, https://doi.org/10.1029/RG001i002p00177.

Hasselmann, S., and K. Hasselmann, 1985a: Computations and parameterizations of the nonlinear energy transfer in a gravity-wave spectrum. Part I: A new method for efficient computations of the exact nonlinear transfer integral. *J. Phys. Oceanogr.*, **15**, 1369–1377, https://doi.org/10.1175/1520-0485(1985)015<1369:CAPOTN>2.0.CO;2.

——, and ——, 1985b: Computations and parameterizations of the nonlinear energy transfer in a gravity-wave spectrum. Part II: Parameterizations of the nonlinear energy transfer for application in wave models. *J. Phys. Oceanogr.*, **15**, 1378–1391, https://doi.org/10.1175/1520-0485(1985)015<1378:CAPOTN>2.0.CO;2.

Hughes, B., 1976: Estimates of underwater sound (and infrasound) produced by nonlinearly interacting ocean waves. *J. Acoust. Soc. Amer.*, **60**, 1032–1039, https://doi.org/10.1121/1.381203.

Hwang, P. A., D. W. Wang, E. J. Walsh, W. B. Krabill, and R. N. Swift, 2000: Airborne measurements of the wavenumber spectra of ocean surface waves. Part II: Directional distribution. *J. Phys. Oceanogr.*, **30**, 2768–2787, https://doi.org/10.1175/1520-0485(2001)031<2768:AMOTWS>2.0.CO;2.

Janssen, P. A. E. M., 1989: Wave-induced stress and drag of air flow over sea waves. *J. Phys. Oceanogr.*, **19**, 745–754, https://doi.org/10.1175/1520-0485(1989)019<0745:WISATD>2.0.CO;2.

——, 1991: Quasi-linear theory of wind-wave generation applied to wave forecasting. *J. Phys. Oceanogr.*, **21**, 1631–1642, https://doi.org/10.1175/1520-0485(1991)021<1631:QLTOWW>2.0.CO;2.

Komen, G. J., S. Hasselmann, and K. Hasselmann, 1984: On the existence of a fully developed wind-sea spectrum. *J. Phys. Oceanogr.*, **14**, 1271–1285, https://doi.org/10.1175/1520-0485(1984)014<1271:OTEOAF>2.0.CO;2.

Lenain, L., and W. K. Melville, 2017: Measurements of the directional spectrum across the equilibrium saturation ranges of wind-generated surface waves. *J. Phys. Oceanogr.*, **47**, 2123–2138, https://doi.org/10.1175/JPO-D-17-0017.1.

——, N. M. Statom, and W. K. Melville, 2019: Airborne measurements of surface wind and slope statistics over the ocean. *J. Phys. Oceanogr.*, **49**, 2799–2814, https://doi.org/10.1175/JPO-D-19-0098.1.

Liu, Q., W. E. Rogers, A. V. Babanin, I. R. Young, L. Romero, S. Zieger, F. Qiao, and C. Guan, 2019: Observation-based source terms in the third-generation wave model WAVE-WATCH III: Updates and verification. *J. Phys. Oceanogr.*, **49**, 489–517, https://doi.org/10.1175/JPO-D-18-0137.1.

Long, C. E., and D. T. Resio, 2007: Wind wave spectral observations in Currituck Sound, North Carolina. *J. Geophys. Res.*, **112**, C05001, https://doi.org/10.1029/2006JC003835.

Longuet-Higgins, M. S., 1950: A theory of the origin of microseisms. *Philos. Trans. Roy. Soc.*, **A243**, 1–35, https://doi.org/10.1098/rsta.1950.0012.

——, 1976: On the nonlinear transfer of energy in the peak of a gravity-wave spectrum: A simplified model. *Proc. Roy. Soc.*, **347A**, 311–328, https://doi.org/10.1098/rspa.1976.0003.

Munk, W., 2009: An inconvenient sea truth: Spread, steepness, and skewness of surface slopes. *Annu. Rev. Mar. Sci.*, **1**, 377–415, https://doi.org/10.1146/annurev.marine.010908.163940.

Peureux, C., A. Benetazzo, and F. Ardhuin, 2018: Note on the directional properties of meter-scale gravity waves. *Ocean Sci.*, **14**, 41–52, https://doi.org/10.5194/os-14-41-2018.

——, F. Ardhuin, and P. V. Guimarães, 2021: On the unsteady steepening of short gravity waves near the crests of longer waves in the absence of generation or dissipation. *J. Geophys. Res. Oceans*, **126**, e2020JC016735, https://doi.org/10.1029/2020JC016735.

Phillips, O. M., 1957: On the generation of waves by turbulent wind. *J. Fluid Mech.*, **2**, 417, https://doi.org/10.1017/S0022112057000233.

——, 1985: Spectral and statistical properties of the equilibrium range in wind-generated gravity waves. *J. Fluid Mech.*, **156**, 505–531, https://doi.org/10.1017/S0022112085002221.

Rogers, E. W., A. V. Babanin, and D. W. Wang, 2012: Observation-consistent input and whitecapping dissipation in a model for wind-generated surface waves: Description and simple calculations. *J. Atmos. Oceanic Technol.*, **29**, 1329–1346, https://doi.org/10.1175/JTECH-D-11-00092.1.

Romero, L., 2019: Distribution of surface wave breaking fronts. *Geophys. Res. Lett.*, **46**, 10463–10474, https://doi.org/10.1029/2019GL083408.

——, and W. K. Melville, 2010a: Airborne observations of fetch-limited waves in the Gulf of Tehuantepec. *J. Phys. Oceanogr.*, **40**, 441–465, https://doi.org/10.1175/2009JPO4127.1.

——, and ——, 2010b: Numerical modeling of fetch-limited waves in the Gulf of Tehuantepec. *J. Phys. Oceanogr.*, **40**, 466–486, https://doi.org/10.1175/2009JPO4128.1.

——, and ——, 2011: Spatial statistics of the sea surface in fetch-limited conditions. *J. Phys. Oceanogr.*, **41**, 1821–1841, https://doi.org/10.1175/2011JPO4535.1.

——, ——, and J. M. Kleiss, 2012: Spectral energy dissipation due to surface wave breaking. *J. Phys. Oceanogr.*, **42**, 1421–1444, https://doi.org/10.1175/JPO-D-11-072.1.

Sutherland, P., and W. K. Melville, 2013: Field measurements and scaling of ocean surface wave-breaking statistics. *Geophys. Res. Lett.*, **40**, 3074–3079, https://doi.org/10.1002/grl.50584.

Toffoli, A., M. Onorato, E. M. Bitner-Gregersen, and J. Monbaliu, 2010: Development of a bimodal structure in ocean wave spectra. *J. Geophys. Res.*, **115**, C03006, https://doi.org/10.1029/2009JC005495.

Tracy, B., and D. T. Resio, 1982: Theory and calculation of the nonlinear energy transfer between sea waves in deep water. WIS Tech. Rep. 11, Hydraulics Lab, U.S. Army Engineer Waterways Experiment Station, 50 pp., https://apps.dtic.mil/sti/pdfs/ADA117989.pdf.

van Vledder, G. P., 2006: The WRT method for the computation of non-linear four-wave interactions in discrete spectral wave models. *Coast. Eng.*, **53**, 223–242, https://doi.org/10.1016/j.coastaleng.2005.10.011.

WW3DG, 2019: User manual and system documentation of WAVEWATCH III version 6.07. Tech. Rep., NOAA/NWS/NCEP/MMAB Tech. Note 333, 465 pp.

Young, I. R., 1995: The determination of confidence limits associated with estimates of the spectral peak frequency. *Ocean Eng.*, **22**, 669–686, https://doi.org/10.1016/0029-8018(95)00002-3.

——, and G. P. Van Vledder,1993: A review of the central role of nonlinear interactions in wind-wave evolution. *Philos. Trans. Roy. Soc.*, **A342**, 505–524, https://doi.org/10.1098/rsta.1993.0030.

——, L. A. Verhagen, and M. L. Banner, 1995: A note on the bimodal directional spreading of fetch-limited wind waves. *J. Geophys. Res.*, **100**, 773–778, https://doi.org/10.1029/94JC02218.

Zieger, S., A. V. Babanin, W. Erick Rogers, and I. R. Young, 2015: Observation-based source terms in the third-generation wave model WAVEWATCH. *Ocean Modell.*, **96**, 2–25, https://doi.org/10.1016/j.ocemod.2015.07.014.